CrossMark

Snapshots of an Evolving Solar Nebula Recorded in Nucleosynthetic Sr and Ba Signatures of Early Condensates

R. T. C. Marquez[1] , B. L. A. Charlier[2] , and F. L. H. Tissot[1]
[1] The Isotoparium, Division of Geological and Planetary Sciences, California Institute of Technology, Pasadena, CA 91125, USA; marquez@caltech.edu
[2] School of Geography, Environment and Earth Sciences, Victoria University of Wellington, Kelburn Parade, Wellington 6140, New Zealand

Abstract

The discovery of extreme strontium isotope anomalies (μ^{84}Sr) in refractory leachates from Allende fine-grained calcium-aluminum-rich inclusions (CAIs) is at odds with long-standing predictions regarding the homogenization of presolar components in the CAI-forming region. Elucidating the stellar source(s) of these phases and the mechanisms for their preservation holds potential significance in understanding the dynamics and evolution of the protoplanetary disk. Here we present barium isotope data for the same set of leachates previously analyzed for μ^{84}Sr. Our results show fairly homogeneous Ba isotope anomalies across leachates ($\sim$100–200 ppm variability), in contrast to the observed μ^{84}Sr variations (up to $\sim$8%). Secondary phases extracted in earlier leaching steps (L1 and L3) reveal trends in μ^{137}Ba and μ^{138}Ba akin to that of mainstream SiC and a second nucleosynthetic component. We show that SiC X grains from Type II supernovae are good end-member candidates for explaining the intra-leachate spread in L1 and L3 μ^{13x}Ba. Notably, neither s-variability nor X-variability appears to contribute to trends in the barium isotope anomalies of the most refractory components (L4 and L5). We propose that the contrast in isotope anomaly systematics between the labile and refractory leachates could reflect a shift in the nucleosynthetic signatures of reservoirs sampled by these components. These observations are consistent with extreme ^{84}Sr p-excesses manifesting only in L4 and L5 leachates. Finally, the decoupled Sr and Ba isotope anomalies point to a nucleosynthetic source that significantly overproduces strontium relative to barium, such as electron-capture supernovae or the collapse of rotating massive stars.

Unified Astronomy Thesaurus concepts: Cosmochemistry (331); Solar system evolution (2293); Meteorites (1038); Chondrites (228)

1. Introduction

The heterogeneity in the chemical and isotopic composition of early solar system (ESS) materials is a testament to the complex evolutionary history of the protosolar nebula. Nucleosynthetic isotope anomalies, which are stellar signatures that manifest as deviations from mass-dependent isotope effects (Dauphas & Schauble 2016), serve as powerful tracers for understanding the dynamics that led to such heterogeneity. One of the more significant recent examples of the importance of nucleosynthetic anomalies is the discovery of a fundamental isotopic dichotomy between bulk carbonaceous (CC) and non-carbonaceous (NC) meteorites (Warren 2011; Budde et al. 2016). This NC–CC dichotomy demonstrates how large-scale features such as spatially segregated reservoirs in the ESS can manifest as distinct isotopic trends (Kleine et al. 2020; Yap & Tissot 2023).

Establishing the degree of isotopic heterogeneity in the nascent nebula is key to gaining insights into the nucleosynthetic heritage of the solar system (Nittler & Ciesla 2016), our interpretation of short-lived radionuclides as relative chronometers for various solar system materials (e.g., ^{26}Al-^{26}Mg; Larsen et al. 2020; Desch et al. 2023), and how disk evolution has shaped the composition of planetary bodies (Lichtenberg et al. 2021; Morbidelli et al. 2022). To this end, a type of refractory inclusion in carbonaceous chondrites known as calcium-aluminum-rich inclusions (CAIs) serves as a prime target for study, as they are considered to be the oldest materials formed in the solar system (Bouvier & Wadhwa 2010; Connelly et al. 2012; Kita et al. 2013). A specific subgroup classified as fine-grained (aka spinel-rich) CAIs (fg-CAIs), widely regarded as products of nebular condensation and re-processing (Davis & Grossman 1979; Hu et al. 2021), are particularly useful in deciphering the processes that shaped the ESS. Because these inclusions likely never experienced remelting, fg-CAIs potentially preserve signatures reflective of ESS heterogeneity that may have been lost in their coarse-grained (i.e., igneous; Stolper & Paque 1986) counterparts.

Indeed, recent analyses of Allende fg-CAIs show a resolvably wider spread in μ^{84}Sr isotope anomalies relative to coarse-grained CAIs (cg-CAIs; Charlier et al. 2019; Masuda & Yokoyama 2023). The larger variance in μ^{84}Sr of fg-CAIs may be due to the preservation of highly anomalous p-carriers, which have been shown to survive as the most refractory leachates from these inclusions (Charlier et al. 2021). Here we leverage high-impedance ($10^{13}\Omega$) amplifiers on a thermal ionization mass spectrometer (TIMS) to characterize the barium (Ba) isotopic composition of the same leachates previously measured for Sr by Charlier et al. Like strontium, barium is an alkali earth metal with a near-identical ionic radius ($\sim$1.5 Å) and would thus be expected to have similar chemical/mineralogical affinities. Such analogous cosmochemical behavior between Sr and Ba manifests in their near-identical condensation temperatures (50% $T_c = 1464$ and 1455 K, respectively; Lodders 2003), as well as similarities in fluid mobility as evidenced by their co-enrichment in terrestrially altered meteorites (Crozaz et al. 2003). The isotope anomalies

Table 1
Five-step Leaching Protocol Previously Applied by Charlier et al. (2021) to fg-CAIs from the Allende Meteorite

Step	Acid	Temp. (°C)	Duration (days)
L1	0.5 M CH_3COOH	20	1
L2	0.5 M HNO_3	20	3
L3	6 M HCl	120	1
L4	14 M HF + 9 M HNO_3	120	1
L5	14 M HF + 9 M HNO_3	220	3
	(in a high-press. Parr bomb)		

for Sr and Ba have also been shown to covary in presolar mainstream SiC (Stephan et al. 2018, 2019), as well as models that predict the production of neutron-rich nuclides during explosive nucleosynthesis (i.e., Type Ia supernovae, Travaglio et al. 2011; and Type II supernovae, Rauscher et al. 2002). In theory, the seven isotopes of barium should reveal additional information regarding the nucleosynthetic heritage of the refractory carriers in fg-CAIs that may be obfuscated by the limitations of the strontium isotope system (i.e., the radiogenic excess from [87]Rb-decay, and possible ambiguity from interpreting the lone [84]Sr anomaly; Moynier et al. 2012).

Our results reveal a lack of pronounced Ba nucleosynthetic anomalies in the most refractory leachates, in contrast with the Sr isotope signatures (Section 3). Using both the elemental and isotopic data on the leachates, we discuss the history of the various components of refractory inclusions and how these may be reflective of ESS dynamics/evolution. We show that a multiplicity of presolar end-members is required in order to explain the nucleosynthetic signatures of these leachates (Section 4.1). Here we argue that these isotopic anomalies are derived (at least partially) from nebular processes such as recondensation and gas–solid reactions in a reservoir relatively enriched in supernova-derived materials (Section 4.2). We also discuss the shifts in trends observed for Ba isotope anomalies across fg-CAI components, as well as how these may be reflective of the disk's compositional evolution (Section 4.3). Lastly, we explore the potential stellar environments that could have led to such decoupling of Ba and Sr isotope anomalies (Section 4.4).

2. Samples and Methods

Here we have analyzed the Ba isotope composition of the same suite of nine fg-CAIs from Charlier et al. (2021). The general mineralogy of each CAI is that of a typical fine-grained inclusion in CV3 meteorites, which is composed mostly of spinel cores surrounded by rims of Al-diopside, as well as minor amounts of other primary condensate phases such as melilite, anorthite, hibonite, and perovskite (Krot et al. 2004). Secondary phases such as nepheline and sodalite with minor amounts of grossular and ferroan olivine are also present and evenly dispersed throughout the CAIs. The outer rims of these irregularly shaped inclusions also host significant amounts of Fe-rich phases such as hedenbergite, ilmenite, and chromite. Some notable exceptions to these general features are *Erik*, which has a relatively high abundance of hibonite (see Figure S2 in Charlier et al. 2021), and *Logan*, which hosts little to no spinel (Figure S5 in Charlier et al. 2021).

As described in Charlier et al., each CAI was subjected to a five-step leaching procedure outlined in Table 1. After each leaching step, small aliquots of the residue powders were collected using acid-cleaned pipette tips and analyzed using the field emission scanning electron microscope (ZEISS 1550 VP) at Caltech (Figure 1). This allowed us to track the minerals that were digested in each step, which are summarized in Table 2. Briefly, nepheline and sodalite were digested during the first two leaching steps. Fe-rich olivine may have seen partial dissolution in L1, followed by complete or near-complete dissolution in L2. Most Ca-rich silicates, such as hedenbergite, grossular, and possibly some melilite and anorthite, experienced significant dissolution during L3. The remaining silicates, mostly Al-diopside with some melilite and anorthite, were digested in L4. Refractory oxides such as spinel and hibonite (and presumably other oxides such as perovskite, magnetite, ilmenite, and chromite) were digested in L5, along with residual fluorides precipitated in the previous step.

Barium is expected to elute as part of the matrix cut during Sr Spec column chromatography (Horwitz et al. 1992) as described in Charlier et al. (2006). Indeed, after recombining the matrix cuts from the previous spiked and unspiked Sr analyses by Charlier et al. (2021), we found a near-complete (85%–100%) recovery of Ba for 36 out of the 44 leachates. Six of the remaining eight samples (L1: *Hank* and *Ororo*; L3: *Peter*; L4: *Peter*; L5: *Jean* and *Peter*) lost somewhere between ~20% and 70% of the initial Ba, while two L4 samples had a significant amount of contamination (~7–10 × the initial sample Ba content). The total procedural blanks for L1–L3 are estimated to be below 40 pg, which corresponds to <1% of the total barium in these samples. As such, the data presented in Table 3 were not corrected for blanks given its minimal contribution to the observed signatures. The blanks for L4 and L5 are estimated to be slightly higher (up to ~200 pg), likely due to the higher acid concentrations and temperatures used for digestion. However, it is worth noting that the difference in the size of vials used for storing the blanks (15 mL PFA) versus those used for leachate samples (7 mL PFA) may also result in overestimated blanks. This is evident from L5 samples *Hank* and *Peter*, where the total recovered Ba is much less than 200 pg.

Varying amounts of the USGS BIR-1a geostandard were processed alongside the CAI leachates. The leachates and geostandard solutions were dried down and brought back to solution using 400 μL of 2 M HNO_3. To purify Ba from the rest of the matrix elements, all samples were subjected to two to three stages of a modified Sr Spec chromatographic separation following the design from Deniel & Pin (2001). This chemistry uses a weaker acid (2 M HNO_3) for eluting the matrix elements, followed by an intermediate 6 M HNO_3 step to collect barium separately from strontium. All of the purified Ba solutions were loaded on outgassed zone-refined Re filaments. A double-filament configuration was used for all samples except for the L5 leachates from *Hank*, *Jean*, and *Peter*. These smaller samples (<150 pg) were loaded on single filaments using a Ta_2F_5 activator (Charlier et al. 2006) and measured at much lower voltages (Table 3).

All measurements were made with the Thermo Finnigan Triton TIMS at the Victoria University of Wellington. All of the analyses were done in static mode with at least 400 cycles with a 16.777 s integration time measuring either ~1.5 V or ~3 V on the major isotope [138]Ba. For the smaller loads typical of L4 and
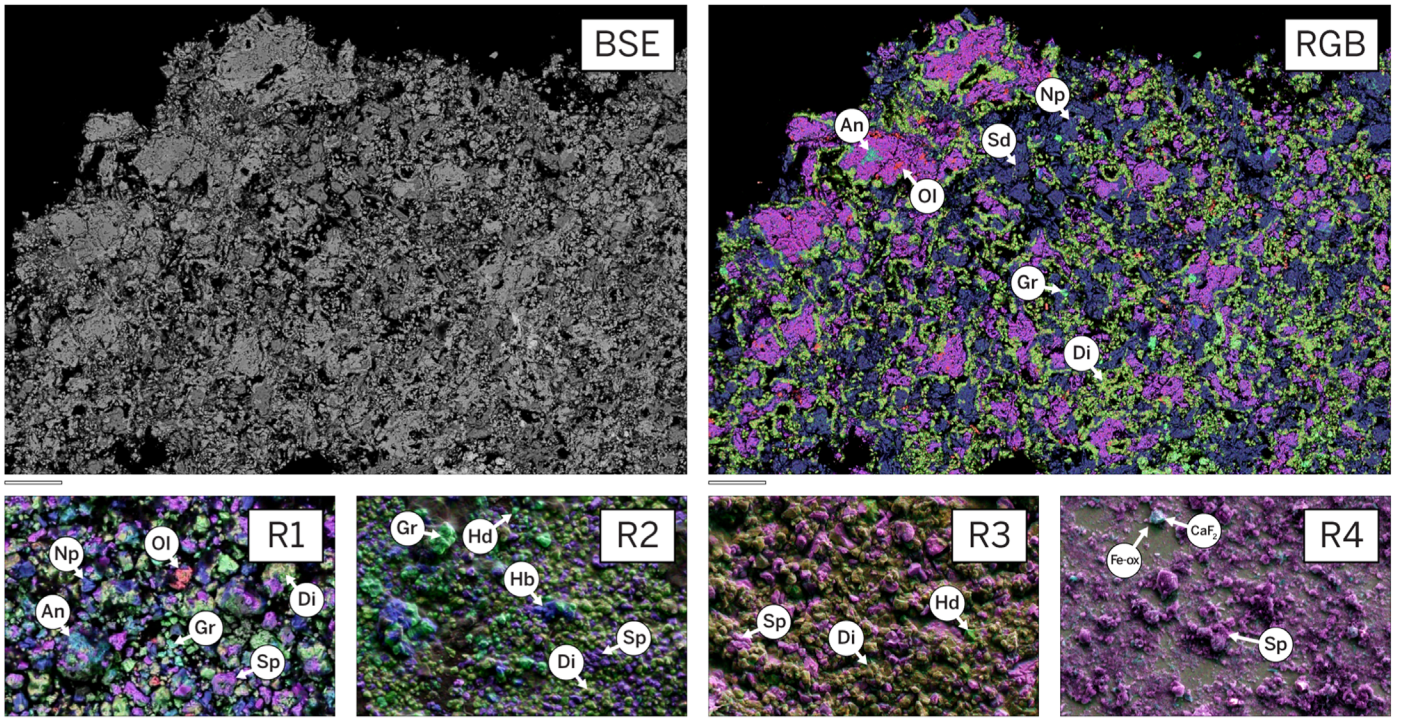
Figure 1. Top: back-scattered electron (BSE) and false-color energy-dispersive X-ray map (red: Mg; green: Ca; blue: Al) of an unprocessed chip of the inclusion *Charles* (μ^{84}Sr = + 1738 ppm), showing the typical mineralogy of a fg-CAI from Allende. Bottom: false-color maps (similar RGB designation to that given above) of leaching residues from the fg-CAI *Ororo* (μ^{84}Sr = + 11599 ppm) for all leaching steps (R1–R4). The following abbreviations are used: Np—nepheline; Sd—sodalite; Ol—(Fe-rich) olivine; An—anorthite; Gr—grossular; Hd—hedenbergite; Hb—hibonite; Di—Al-diopside; Sp—spinel; Fe-ox—iron oxide. Specks with a teal false color in R4, identified to be calcium fluoride (CaF$_2$), were precipitated from HF and dissolved Ca-rich phases during L4. A scale bar denoting 50 μm is shown in the lower left corner of each image.

Table 2
Occurrence of Major Phases in fg-CAI Residues (R1–R4) Produced after Each Step of the Leaching Protocol

Mineral	R1	R2	R3	R4
nepheline	◑	○	⋯	⋯
sodalite	◑	○	⋯	⋯
olivine	●	○	⋯	⋯
grossular	●	●	◑	○
hedenbergite	●	●	◑	○
anorthite	●	●	◑	○
melilite	●	●	?[a]	○
Al-diopside	●	●	●	○[b]
hibonite	●	●	●	●
spinel	●	●	●	●
perovskite	●	●	●	?[c]

Notes. The following symbols are used: ●—preserved, little to no dissolution; ◑—present, but with lower relative abundance, partial dissolution; ○—undetected or present in trace amounts, complete or near-complete dissolution; ?—likely to survive but unverified owing to low initial abundance.
[a] Melilite occurs in small amounts even prior to dissolution and was thus difficult to detect among other Ca-rich phases.
[b] Al-diopside was fully dissolved but with some reprecipitation of material as fluorides (see Figure 1).
[c] Perovskite was present in trace amounts but presumed to survive along with other oxides (i.e., hibonite, spinel).

L5 leachates, the amount of analyte available dictated the number of cycles and average measurement voltages. Five $10^{13}\Omega$ amplifiers were used to measure the least abundant isotopes:

^{130}Ba (0.11%), ^{132}Ba (0.10%), ^{134}Ba (2.42%), ^{135}Ba (6.59%), and ^{136}Ba (7.85%). Four $10^{11}\Omega$ amplifiers were used to collect the relatively abundant ^{137}Ba (11.2%) and ^{138}Ba (71.7%) isotopes, as well as to monitor ^{139}La and ^{140}Ce for direct isobaric interferences on ^{138}Ba (i.e., ^{138}La and ^{138}Ce).

The tau-correction factor (τ) for each amplifier was empirically determined for these sessions. This was done using a beam from a double filament loaded with the NIST 3104a terrestrial standard. The filament was tuned to have 3 V on ^{138}Ba in order to match the sample measurement conditions. After tuning, a sequence of $n = 6500$ cycles with 8 μs integrations was started, during which the analyzer gate was closed to capture the individual amplifier transients. The data were made to fit the exponential offset equation as described by Craig et al. (2017):

$$I = I_{\circ} \cdot e^{-\Delta t/\tau},$$

where I_o is the signal intensity prior to closing the analyzer gate (i.e., ~3 V) and Δt is the time elapsed by the signal decay. All of the measured barium isotope ratios were internally normalized to ^{134}Ba/^{136}Ba = 0.307776 (Yobregat et al. 2017) using the exponential law (Russell et al. 1978) and expressed as parts-per-million (ppm) deviations (μ^{13x}Ba) relative to voltage-matched measurements of the NIST 3104a standard (Table 4):

$$\mu^{13x}\mathrm{Ba} = \left(\frac{^{13x}\mathrm{Ba}/^{136}\mathrm{Ba}_{\mathrm{sample}}}{^{13x}\mathrm{Ba}/^{136}\mathrm{Ba}_{\mathrm{NIST\ 3104a}}} - 1 \right) \times 10^6.$$

Table 3
Barium Isotope Ratios of the Leachates Derived from Allende fg-CAIs

Sample	Initial Ba (ng)	Recovered Ba (ng)	Volts ^{138}Ba	N	β	^{130}Ba/^{136}Ba	^{132}Ba/^{136}Ba	^{135}Ba/^{136}Ba	^{137}Ba/^{136}Ba	^{138}Ba/^{136}Ba	^{138}Ba/^{136}Ba$_c$
L1											
Charles	59.55	57.995	1.52	380	0.3485	0.0134786 (17)	0.0128998 (14)	0.839330 (8)	1.429134 (21)	9.13040 (17)	9.13035
Erik	77.89	66.511	2.99	475	0.1897	0.0134832 (8)	0.0129014 (8)	0.839329 (6)	1.429211 (13)	9.13072 (12)	9.13067
Hank	36.44	11.807	2.77	380	0.0085	0.0134814 (10)	0.0129009 (10)	0.839337 (7)	1.429250 (16)	9.13079 (14)	9.13078
Jean	20.49	20.232	2.95	361	0.1091	0.0134824 (9)	0.0129027 (9)	0.839324 (7)	1.429231 (15)	9.13050 (12)	9.13043
Logan	12.57	14.050	2.99	418	0.0323	0.0134832 (9)	0.0129014 (9)	0.839342 (6)	1.429229 (13)	9.13081 (11)	9.13076
Ororo	68.42	61.528	3.04	437	0.2565	0.0134806 (9)	0.0129010 (8)	0.839325 (6)	1.429251 (13)	9.13083 (11)	9.13075
Peter	21.22	16.246	2.96	380	0.0828	0.0134840 (9)	0.0129013 (8)	0.839319 (6)	1.429154 (14)	9.13043 (12)	9.13038
Raven	20.12	20.251	2.93	437	0.0881	0.0134813 (9)	0.0129017 (8)	0.839346 (6)	1.429197 (13)	9.13067 (11)	9.13053
Scott	68.82	65.248	3.10	475	0.3136	0.0134823 (8)	0.0129009 (8)	0.839330 (6)	1.429241 (13)	9.13082 (11)	9.13082
L2											
Charles	44.31	49.613	3.04	475	0.2683	0.0134833 (9)	0.0129024 (7)	0.839338 (5)	1.429148 (14)	9.13047 (12)	9.13045
Erik	28.91	31.198	1.89	380	0.1140	0.0134839 (12)	0.0129040 (12)	0.839326 (8)	1.429143 (18)	9.12987 (16)	9.12984
Hank	12.12	13.756	1.96	380	−0.0087	0.0134860 (13)	0.0129024 (13)	0.839339 (8)	1.429104 (22)	9.12955 (19)	9.12954
Jean	10.57	11.817	1.56	285	0.0153	0.0134808 (17)	0.0129006 (16)	0.839320 (10)	1.429202 (22)	9.12970 (20)	9.12967
Logan	8.03	8.965	2.82	380	−0.0672	0.0134856 (11)	0.0129017 (9)	0.839341 (6)	1.429141 (15)	9.13055 (14)	9.13050
Ororo	66.38	68.402	3.05	760	0.1826	0.0134828 (7)	0.0129012 (6)	0.8394665 (4)	1.429122 (10)	9.13046 (8)	9.13042
Raven	11.32	13.558	1.25	722	0.1807	0.0134877 (13)	0.0129024 (12)	0.839352 (7)	1.428977 (16)	9.12982 (15)	9.12973
Scott	84.80	87.223	3.46	380	0.3285	0.0134847 (8)	0.0129022 (7)	0.839333 (6)	1.429262 (13)	9.13064 (11)	9.13063
L3											
Charles	150.53	137.279	3.18	380	0.3131	0.0134819 (8)	0.0129002 (8)	0.839340 (6)	1.429217 (14)	9.13090 (11)	9.13017
Erik	200.96	193.852	3.11	380	0.3089	0.0134824 (9)	0.0129027 (8)	0.839332 (6)	1.429194 (13)	9.13043 (12)	9.13031
Hank	15.88	16.432	2.85	323	−0.2700	0.0134843 (11)	0.0129017 (10)	0.839342 (7)	1.429168 (15)	9.13040 (14)	9.13012
Jean	31.60	37.081	2.92	380	0.0247	0.0134834 (9)	0.0129003 (9)	0.839327 (6)	1.429181 (15)	9.13067 (12)	9.13017
Logan	17.84	18.093	2.82	380	−0.1725	0.0134791 (10)	0.0128998 (8)	0.839341 (6)	1.429210 (15)	9.13073 (12)	9.13035
Ororo	329.25	292.850	3.14	380	0.3152	0.0134817 (8)	0.0129022 (8)	0.839335 (6)	1.429202 (13)	9.13076 (12)	9.13035
Peter	43.14	27.918	2.98	380	0.2178	0.0134850 (9)	0.0129027 (8)	0.839331 (6)	1.429150 (13)	9.13056 (13)	9.12998
Raven	54.96	51.076	3.06	380	0.3162	0.0134834 (9)	0.0129006 (8)	0.839360 (6)	1.429219 (14)	9.13120 (12)	9.13026
Scott	640.09	583.886	3.00	380	0.4228	0.0134812 (9)	0.0129006 (8)	0.839339 (6)	1.429181 (14)	9.13026 (12)	9.13024
L4											
Charles	0.12	1.325	0.15	76	0.0228	0.0134951 (304)	0.0129064 (274)	0.839318 (75)	1.429328 (250)	9.12929 (183)	9.12929
Erik	54.74	58.792	2.88	418	0.1913	0.0134832 (9)	0.0129015 (9)	0.839343 (6)	1.429201 (21)	9.13051 (17)	9.13036
Hank	0.97	1.150	0.12	58	−0.0474	0.0135311 (416)	0.0129690 (439)	0.839182 (126)	1.428938 (403)	9.13200 (269)	9.13200
Jean	0.92	1.255	0.13	115	−0.0613	0.0134913 (301)	0.0129408 (328)	0.839369 (76)	1.428392 (223)	9.13049 (178)	9.12844
Logan	4.47	4.796	1.37	152	−0.0010	0.0134830 (27)	0.0129036 (25)	0.839353 (15)	1.429081 (38)	9.13014 (30)	9.13011
Ororo	0.08	0.600	0.13	399	0.0605	0.0135108 (137)	0.0129577 (140)	0.839409 (36)	1.429659 (108)	9.13317 (79)	9.13179
Peter	3.40	1.457	0.12	152	0.1136	0.0134868 (247)	0.0128920 (217)	0.839404 (65)	1.429239 (161)	9.13168 (136)	9.13106
Raven	5.26	6.542	1.03	95	0.0190	0.0134853 (45)	0.0129000 (33)	0.839360 (21)	1.429074 (64)	9.13070 (50)	9.12969
Scott	3.37	3.860	1.39	304	0.1111	0.0134794 (20)	0.0129006 (17)	0.839341 (11)	1.429067 (25)	9.12947 (23)	9.12947
L5											
Charles	7.56	8.826	2.55	152	0.0704	0.0134821 (17)	0.0128991 (15)	0.839324 (10)	1.429093 (27)	9.13086 (22)	9.13031
Erik	13.38	12.794	2.92	304	0.0631	0.0134824 (11)	0.0129010 (10)	0.839342 (7)	1.429139 (16)	9.13070 (13)	9.13034
Hank	0.08	0.086	0.03	47	−0.1171	0.0135012 (2181)	0.0130654 (3155)	0.839418 (537)	1.429465 (1252)	9.12913 (667)	9.12893
Ororo	5.76	6.142	1.49	323	0.1092	0.0134816 (18)	0.0128990 (17)	0.839368 (9)	1.429047 (28)	9.13134 (23)	9.12902
Peter	0.19	0.133	0.05	96	−0.0570	0.0136617 (694)	0.0129382 (712)	0.839390 (152)	1.430306 (478)	9.13464 (430)	9.13439
Raven	7.59	7.656	1.54	532	0.0960	0.0134818 (13)	0.0129002 (12)	0.839367 (8)	1.429081 (16)	9.13121 (15)	9.12978
Scott	9.18	9.266	1.38	399	0.1114	0.0134851 (16)	0.0128989 (16)	0.839345 (9)	1.429052 (21)	9.12989 (18)	9.12979

Note. All of the presented ratios were derived after internal normalization to ^{134}Ba/^{136}Ba = 0.307776 (Yobregat et al. 2017). The mass-dependent fractionation is corrected using the exponential law (Russell et al. 1978) and expressed here as the fractionation factor, β. The ^{138}Ba/^{136}Ba ratios corrected for ^{138}La decay (Section 2) are shown here as a separate column (^{138}Ba/^{136}Ba$_c$).

3. Results

The internally normalized barium isotope ratios for the Allende fg-CAI leachates are summarized in Table 3. Figure 2 shows the nucleosynthetic isotope anomalies expressed as μ values for all nonnormalizing isotopes (^{130}Ba, ^{132}Ba, ^{135}Ba, ^{137}Ba, and ^{138}Ba) across the different leaching steps for samples that were measured with at least 1.5 V on ^{138}Ba. Note that the quoted errors for these μ^{13x}Ba values are dominated by the propagated external reproducibility calculated from multiple voltage-matched measurements of the NIST 3104a standard (Table 4).

The μ^{138}Ba anomalies presented here have also been corrected for ^{138}La decay (via ec β^{+}, branching ratio = 65.5%, $\lambda = 6.73 \times 10^{-11}$ yr^{-1}; Kondev et al. 2021) using the following equation:

$$\frac{^{138}\text{Ba}}{^{136}\text{Ba}}_{\text{corr}} = \frac{^{138}\text{Ba}}{^{136}\text{Ba}}_{\text{meas}} - 0.655 \cdot \frac{^{138}\text{La}}{^{136}\text{Ba}} \cdot (e^{\lambda t} - 1).$$

Here we assume that all samples have a similar age of $t = 4.567 \times 10^9$ yr (Connelly et al. 2012). Most L1 and L2 leachates required very little correction to μ^{138}Ba ($\leqslant 5$ ppm) owing to their low La/Ba (<0.30). For the typical L3–L5 leachates that have higher La/Ba ratios of $\sim$2–3, corrections were within $\sim$35–50 ppm. The magnitude of these corrections is similar to those typically applied to bulk cg-CAIs (Brennecka et al. 2013; Shollenberger et al. 2018).

For the relatively larger loads ($\sim$5–580 ng) shown in Figure 2, the nucleosynthetic Ba isotope anomalies appear to be relatively homogeneous across leaching steps. The lone exception is L2, which shows large variations in μ^{135}Ba and μ^{137}Ba that will be discussed as a separate study. In general, however, the average μ^{135}Ba anomalies for these leachates are within uncertainty of each other. The same is true for the μ^{137}Ba and μ^{138}Ba isotope anomalies, albeit with a possible decreasing trend in the former. For the minor isotopes, ^{130}Ba and ^{132}Ba, any nucleosynthetic anomalies, if present, are unresolvable owing to the large associated uncertainties due to their extremely low abundance. This is true even in the most refractory leachates (L4 and L5), which, despite containing large p-excesses in ^{84}Sr, show no resolvable anomalies in Ba p-nuclides (^{130}Ba and ^{132}Ba).

Figure 3 shows the reconstituted bulk isotope anomalies (i.e., weighted average of L1–L5 μ^{13x}Ba) of the fg-CAIs studied here. The average isotope anomaly patterns for Group II and non–Group II Allende CAIs previously measured by Brennecka et al. (2013), which includes both fine-grained and coarse-grained examples, were also superimposed on these patterns. Notably, the barium isotope anomalies for the fg-CAIs and cg-CAIs are within uncertainty of each other, suggesting a shared history between these inclusion subtypes, likely through sampling the same isotopic reservoirs. The signatures from L1–L3 leachates dominate these overall bulk patterns, as they comprise 85%–99% of the total barium budget (see Table 3).

4. Discussion

4.1. Nucleosynthetic Variations Akin to Presolar Carriers

Figure 4 shows cross-plots of the nucleosynthetic isotope variations for L1 and L3 (panels (a)–(c)) and L4 and L5 (panels (d)–(f)). Superimposed on the data is the predicted correlation of Ba isotope anomalies from s-deficit variations based on the composition of mainstream presolar SiC grains (in yellow;

Stephan et al. 2018, 2019) anchored to the terrestrial composition (i.e., μ^{13x}Ba = 0). The μ^{137}Ba versus μ^{138}Ba L3 isotope anomalies (Figure 4(c)) appear to follow this slope tightly, albeit with a slight negative offset in μ^{138}Ba. The slope is also fairly well-defined for L1 leachates, but with considerably larger variability and an apparent positive μ^{138}Ba offset relative to the s-variability trend. Note, however, that L1 and L3 leachates still have positive μ^{13x}Ba anomalies, suggesting that the barium isotope budget is still predominantly characterized by a relative s-deficit and/or r-excess.

In contrast, the correlations between μ^{135}Ba versus μ^{137}Ba (Figure 4(a)) and μ^{135}Ba versus μ^{138}Ba (Figure 4(b)) appear to deviate from the s-deficit trends. Similar to Figure 4(c), however, the same apparent positive and negative offsets in μ^{138}Ba relative to the projected s-variability slope were observed in Figure 4(b) for L1 and L3 leachates, respectively. Taken at face value, this could be the result of erroneous corrections of contributions from ^{138}La decay (i.e., undercorrection on L1 and overcorrection on L3) due to disturbances in the La/Ba ratio. One possible source of shifts in this ratio is the selective enrichment of light rare earth elements (LREEs; i.e., La) during REE remobilization from aqueous alteration (Crozaz et al. 2003). This is unlikely to be the case, however, as similar offsets and intra-leachate clustering of anomalies are also observed in the μ^{135}Ba versus μ^{137}Ba space (Figure 4(a)).

The observed deviations from s-variability in L1 and L3 within the μ^{135}Ba versus μ^{137}Ba (Figure 4(a)) and μ^{135}Ba versus μ^{138}Ba (Figure 4(b)) spaces likely come from the contribution of an additional stellar component. Such a component would need to have predicted ^{137}Ba and ^{138}Ba excesses similar to mainstream SiC to avoid significant deviations from the s-deficit slope in Figure 4(c). At the same time, this component must also exhibit trends in μ^{135}Ba versus μ^{137}Ba and μ^{135}Ba versus μ^{138}Ba that are disparate from those of s-variability in order to explain the spread in Figures 4(a)–(b). The only known presolar carriers that fit these criteria are SiC X grains (Stephan et al. 2018). The predicted slopes for both X1 and X2 grains appear to explain the variability in Figures 4(a)–(c), with L1 leachates exhibiting a relative X-excess and L3 leachates trending toward X-deficits. Indeed, we are able to quantitatively demonstrate that the L1 and L3 anomalies approximately define a 2D plane within the μ^{135}Ba-μ^{137}Ba-μ^{138}Ba space (Appendix A.1) and that the combined s-process and X-grain compositional vectors are able to explain the span of the data (Appendices A.2 and A.3).

4.2. Origin of Nucleosynthetic Signatures of Secondary Phases in fg-CAIs

Generally, X grains constitute only a minor fraction (1%–2%) of presolar SiC and are characterized by low δ^{13}C, δ^{29}Si, and δ^{30}Si along with a high δ^{15}N (Hoppe & Ott 1997; Hoppe et al. 2000). These isotopic signatures have previously been proposed to derive from Type II supernovae (Amari et al. 1992; Davis 2011). It may thus seem peculiar for L1 leachates, which consist of secondary Na- and K-bearing silicates such as nepheline and sodalite, to be relatively enriched in such supernova-derived signatures. We wish to emphasize that the X-excesses in L1 do not require for carriers to be hosted in the silicate alteration rims of fg-CAIs. Indeed, since L1 leachates were collected with a relatively weak acid (0.5 M CH$_3$COOH), it is very unlikely that this step extracted Ba from highly refractory SiC carriers. However, it is important to note that the

Table 4
Barium Isotope Ratios of the NIST 3104a Terrestrial Standard as Measured in Different Conditions and Configurations

Volts ^{138}Ba	N	β	^{130}Ba/^{136}Ba	^{132}Ba/^{136}Ba	^{135}Ba/^{136}Ba	^{137}Ba/^{136}Ba	^{138}Ba/^{136}Ba
			10 ng NIST 3104a at 3 V on ^{138}Ba, Doubles				
2.88	380	0.2639	0.0134814 (10)	0.0129022 (9)	0.839284 (7)	1.429161 (15)	9.13028 (14)
2.95	380	0.2808	0.0134817 (10)	0.0129003 (9)	0.839287 (6)	1.429131 (14)	9.13043 (12)
2.89	380	0.1295	0.0134813 (9)	0.0129009 (9)	0.839290 (7)	1.429167 (13)	9.13057 (12)
2.87	380	0.2348	0.0134815 (9)	0.0129003 (9)	0.839291 (7)	1.429124 (14)	9.13030 (12)
2.92	380	0.2689	0.0134829 (9)	0.0129011 (9)	0.839295 (6)	1.429137 (15)	9.13034 (13)
3.03	380	0.2724	0.0134831 (10)	0.0129023 (8)	0.839291 (6)	1.429149 (14)	9.13042 (12)
2.87	380	0.2583	0.0134845 (109)	0.0129030 (8)	0.839289 (6)	1.429152 (15)	9.13022 (12)
2.91	380	0.0692	0.0134842 (9)	0.0129021 (9)	0.839289 (6)	1.429122 (15)	9.13024 (13)
2.80	380	0.2829	0.0134828 (10)	0.0129016 (9)	0.839293 (6)	1.429128 (13)	9.13021 (12)
3.39	304	0.3084	0.0134810 (9)	0.0129039 (9)	0.839288 (7)	1.429121 (16)	9.13040 (14)
2.93	475	0.2765	0.0134825 (9)	0.0129015 (8)	0.839291 (6)	1.429163 (14)	9.13046 (12)
2.92	779	0.1695	0.0134849 (7)	0.0129044 (6)	0.839301 (5)	1.429153 (10)	9.13003 (9)
3.01	760	0.1803	0.0134836 (7)	0.0129012 (6)	0.839291 (4)	1.429174 (10)	9.13022 (9)
		Mean	0.0134827	0.0129019	0.839291	1.429145	9.13032
		2 s.e.	0.0000026	0.0000025	0.000008	0.000037	0.00028
		2 s.e. (ppm)	193	194	10	26	31
			10 ng NIST 3104a at 1.5 V on ^{138}Ba, Doubles				
1.60	380	0.3180	0.0134842 (15)	0.0129042 (13)	0.839307 (8)	1.429046 (19)	9.12959 (17)
1.59	380	0.3338	0.0134868 (15)	0.0129033 (14)	0.839305 (9)	1.429086 (21)	9.12973 (17)
1.72	380	0.3450	0.0134795 (14)	0.0128994 (13)	0.839297 (8)	1.429094 (19)	9.13041 (16)
1.58	380	0.3460	0.0134846 (15)	0.0129064 (14)	0.839294 (8)	1.429140 (20)	9.13026 (17)
1.40	380	0.3354	0.0134842 (16)	0.0128990 (16)	0.839294 (10)	1.429073 (21)	9.12959 (19)
1.47	380	0.3348	0.0134830 (15)	0.0128995 (15)	0.839289 (9)	1.429032 (19)	9.12965 (16)
1.46	380	0.3060	0.0134835 (16)	0.0129016 (14)	0.839298 (10)	1.429046 (22)	9.12995 (20)
		Mean	0.0134844	0.0129023	0.839298	1.429070	9.12980
		2 s.e.	0.0000026	0.0000057	0.000014	0.000079	0.00053
		2 s.e. (ppm)	193	442	17	55	58
			1 ng NIST 3104a, Doubles				
0.33	304	−0.0534	0.0134807 (75)	0.0129200(62)	0.839301 (24)	1.429330 (64)	9.13014 (55)
0.13	418	0.2022	0.0134708 (157)	0.0129351 (164)	0.839274 (36)	1.428802 (115)	9.13256 (87)
0.19	380	−0.0014	0.0135035 (98)	0.0129144 (104)	0.839258 (31)	1.428978 (79)	9.13034 (64)
0.16	114	−0.2115	0.0135413 (285)	0.0129135 (223)	0.839343 (60)	1.429512 (201)	9.13533 (146)
		Mean	0.0134991	0.0129207	0.839294	1.429155	9.13209
		2 s.e.	0.0000626	0.0000199	0.000074	0.000647	0.00484
		2 s.e. (ppm)	4637	1540	88	453	530
			100 pg NIST 3104a, Singles				
0.09	190	−0.1385	0.0135821 (257)	0.0129415 (255)	0.839323 (70)	1.429425 (194)	9.13046 (135)
0.12	285	−0.1992	0.0134689 (179)	0.0129458 (188)	0.839272 (47)	1.429236 (127)	9.13200 (91)
0.09	133	−0.1455	0.0135130 (354)	0.0129166 (355)	0.839296 (93)	1.430112 (249)	9.13203 (206)
0.11	228	−0.0725	0.0136016 (247)	0.0128996 (212)	0.839281 (59)	1.429015 (153)	9.12894 (119)
0.11	209	−0.0464	0.0134915 (243)	0.0129224 (238)	0.839269 (57)	1.429380 (165)	9.13200 (121)
0.12	209	−0.0430	0.0134647 (217)	0.0129229 (203)	0.839351 (54)	1.429439 (148)	9.12958 (109)
0.11	114	−0.1298	0.0135615 (355)	0.0129079 (311)	0.839290 (75)	1.430275 (265)	9.13349 (173)
		Mean	0.0135262	0.0129224	0.839297	1.429555	9.13121
		2 s.e.	0.0001111	0.0000334	0.000059	0.000925	0.00321
		2 s.e. (ppm)	8214	2585	70	647	352

Note. All of the presented ratios were derived after internal normalization to ^{134}Ba/^{136}Ba = 0.307776 (Yobregat et al. 2017). The mass-dependent fractionation is corrected using the exponential law (Russell et al. 1978) and expressed here as the fractionation factor, β. The grouped means of the ratios for replicate measurements in the same conditions are also shown—these are used to calculate the barium isotope anomaly (μ^{13x}Ba) in samples measured at the same corresponding voltage/configuration (see Section 2). The calculated external reproducibility (2 s.e.) is the standard deviation of replicate standard measurements, and it is also expressed here in ppm.

elemental and isotopic signatures of L1 and L3 are likely to be the confluence of both aqueous alteration and nebular condensation, as the secondary phases digested in these steps were derived from open-system metasomatic reactions involving primary nebular condensates (i.e., melilite, anorthite; Krot et al. 1995). As such, we explore how the observed L1 and L3 signatures may be explained by (1) remobilization of barium from the matrix during parent-body alteration or (2) mineral precursors sampling a gaseous reservoir enriched in X-like

signatures during gas–solid nebular reactions. We discuss the merits and limitations of each interpretation below.

Due to the high amounts of Ba in the Allende matrix (165 ppm vs. 15 ppm in refractory inclusions; Tanaka & Masuda 1973), remobilization via aqueous fluids during parent-body alteration has the potential to overprint the chemical and isotopic signature of relatively porous components such as fg-CAIs. For instance, the high abundance of hedenbergite in Allende fg-CAIs has been proposed to be due
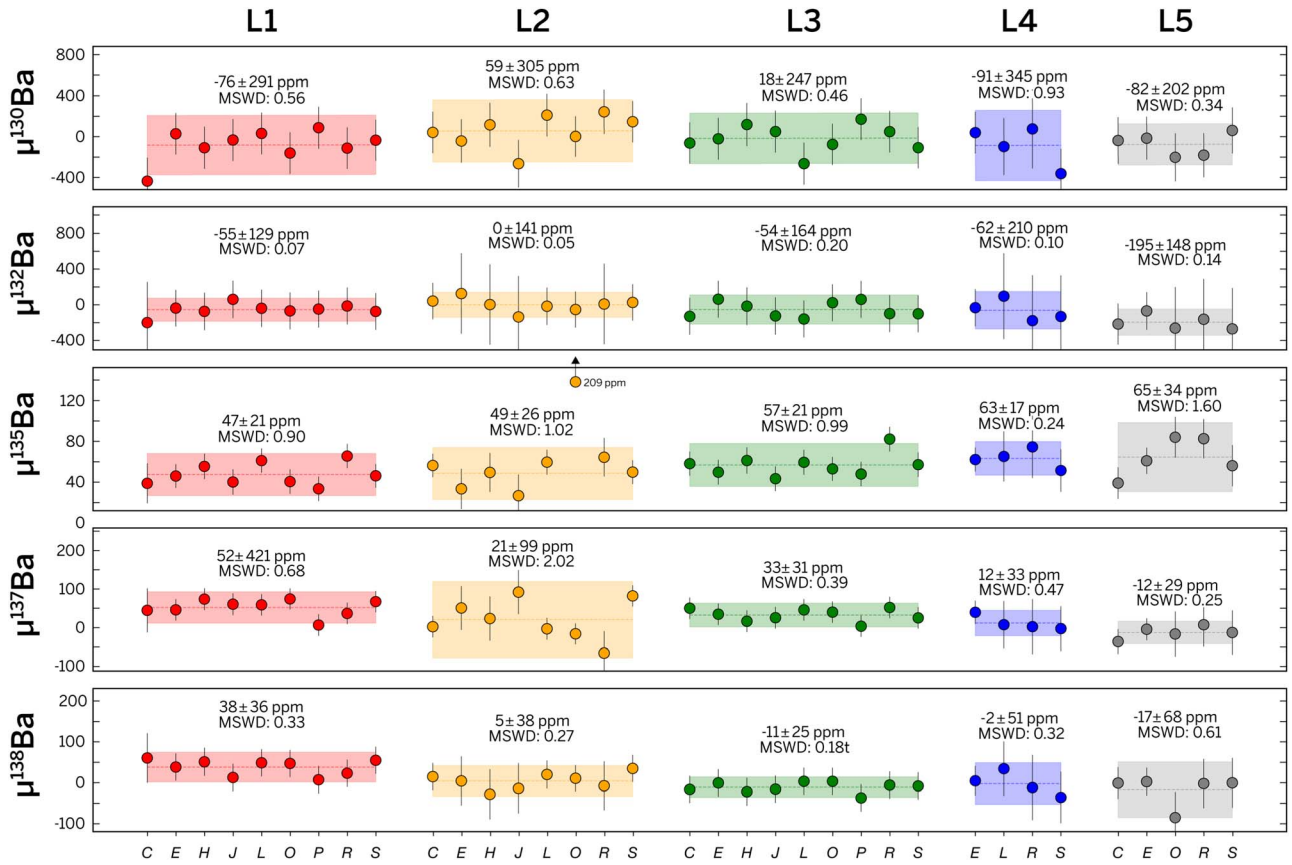
Figure 2. Nucleosynthetic barium isotope anomalies (i.e., μ^{130}Ba, μ^{132}Ba, μ^{135}Ba, μ^{137}Ba, and μ^{138}Ba) in individual leachates from the Allende fg-CAIs previously analyzed for Sr by Charlier et al. (2021). Note that only the samples with enough Ba to be measured with at least ~1.5 V on ^{138}Ba are shown here (see Table 3 for the anomalies on smaller L4 and L5 loads). The mean (colored dashed lines) and corresponding uncertainties (weighted 2 s.d.; shaded areas) for the anomalies on each leaching step are also shown and labeled. Note that the mean for μ^{135}Ba on L2 excludes the relatively extreme values for *Ororo* (μ^{135}Ba= 209 ppm).

to its lower degree of compaction relative to CV3-red meteorites (e.g., Efremovka and Leoville), thus leading to the enhanced effects of metasomatism (macPherson & Krot 2002). This phenomenon appears to manifest in the ε^{94}Mo and ε^{95}Mo isotope anomalies of some Group II inclusions, as they plot along the bulk CC line as opposed to the more *r*-enriched "CAI line" defined by coarse-grained counterparts (Brennecka et al. 2020). To test this, we examine the barium isotope composition of Allende matrix separates (marked with crosses in Figure 4, from Budde et al. 2016) in relation to our fg-CAI data. Here we see that the Allende matrix appears to lie squarely on the *s*-deficit variation line for all three isotope spaces in Figure 4. If we only take μ^{137}Ba versus μ^{138}Ba (Figure 4(c)) variations into account, one can surmise that the trend observed in L1 and L3 leachates may be produced from variable mixing of matrix-derived Ba and an end-member with a relatively larger *r*-excess, presumably representing an unaltered refractory progenitor.

The biggest issue with this interpretation of the L1 and L3 signatures is that it is unable to produce the variations observed in Figures 4(a)–(b). As previously discussed in Section 4.1, these variations require at least one more component in addition to *s*-variability (see Appendix A.1), here suggested to be an X-grain-like component. Matrix-derived Ba appears to strictly follow the mainstream SiC trend and bear no resemblance to X-signatures in μ^{135}Ba versus μ^{137}Ba (Figure 4(a)) and μ^{135}Ba versus μ^{138}Ba (Figure 4(b)) isotope spaces. This aligns with the fact that SiC X grains have thus far

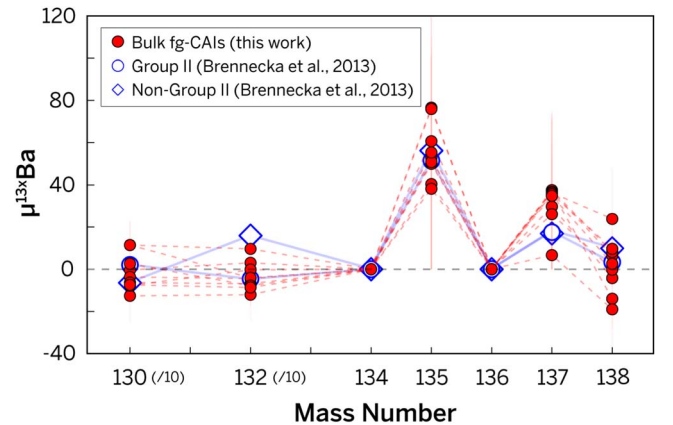**Figure 3.** Reconstituted bulk $\mu^{13\,x}$Ba from the weighted mean of the barium isotope anomalies in individual leachates. The average bulk isotope anomalies in Group II (open circles) and non–Group II cg-CAIs (open diamonds) from Brennecka et al. (2013) are also shown (blue). Note that the isotope anomalies and corresponding uncertainties for ^{130}Ba and ^{132}Ba are divided by 10 in order to fit these values on the same scale as the more abundant barium isotopes.

not been detected in the Allende matrix specifically. As such, remobilized barium from the matrix is unlikely to be the source of variations orthogonal to the mainstream SiC trend—if anything, matrix-derived barium is likely to be a contributor to some of the *s*-variability in these CAI components as observed in Figure 4(c).
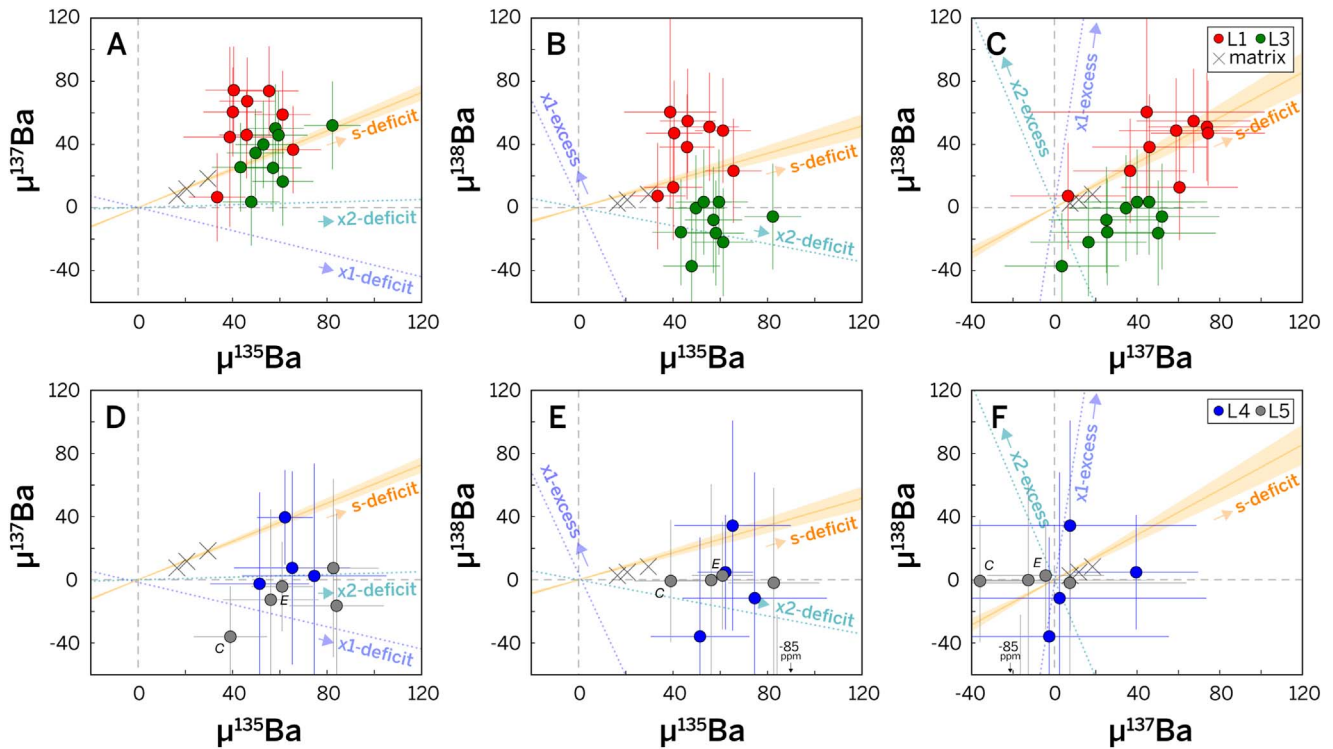
Figure 4. Cross-plots of μ^{135}Ba, μ^{137}Ba, and μ^{138}Ba for L1 and L3 (panels (a)–(c)) and L4 and L5 (panels (d)–(f)) leachates from the Allende fg-CAIs previously analyzed for Sr by Charlier et al. (2021). Expected covariations in barium isotope anomalies from excesses/deficits in s-carriers (mainstream SiC; Stephan et al. 2019) and SiC X grains (X1 and X2; Stephan et al. 2018), anchored to the terrestrial composition ($\mu^{13.x}$Ba = 0), are also shown. The barium isotope anomalies in Allende matrix separates (Budde et al. 2016) are marked with crosses. Specific L5 samples *Charles* (*C*) and *Erik* (*E*) are labeled in support of the discussions in Section 4.3.

We now consider the possibility that X-like nucleosynthetic Ba signatures may have been acquired prior to parent-body accretion. Specifically, we explore how these may be remanent signatures of primary nebular condensates that were preserved in their secondary metasomatic products. Monomineralic layers of Al-diopside, melilite, and anorthite in fg-CAIs from reduced CV3 chondrites such as Efremovka and Leoville were interpreted by Krot et al. (2004) to have formed from low-temperature gas–solid reactions between spinel ± hibonite ± perovskite and a SiO-Mg-rich gas. Melilite and anorthite are particularly susceptible to aqueous alteration and were replaced progressively by grossular, nepheline, and sodalite during parent-body metasomatism (Krot et al. 1995).

The REE patterns for individual leachates appear to support the preservation of nebular signatures in these secondary phases. At the bulk scale, fg-CAIs exhibit a Group II REE pattern, which is defined by depletions in the most refractory REEs (Gd-Er and Lu), as well as the most volatile (Eu and Yb), accompanied by enrichments in moderately refractory REEs (La-Sm and Tm; Mason & Taylor 1982). These patterns, initially thought to be snapshots of the nebular condensation sequence (Davis & Grossman 1979), have since been shown to be from rapid evaporation of early refractory condensates immediately followed by near-equilibrium recondensation (Hu et al. 2021). Analysis of the individual leachates reveals that the Group II pattern appears to be consistently present across leaching steps (Figure 5). It is unlikely that these signatures are solely from intra-CAI redistribution of REEs during aqueous parent-body alteration, as it would be difficult to explain the increase by 2–3 orders of magnitude in REE concentrations for L3 (mostly secondary Ca-rich silicates) relative to the presumed silicate/oxide precursors in L4+L5. The addition
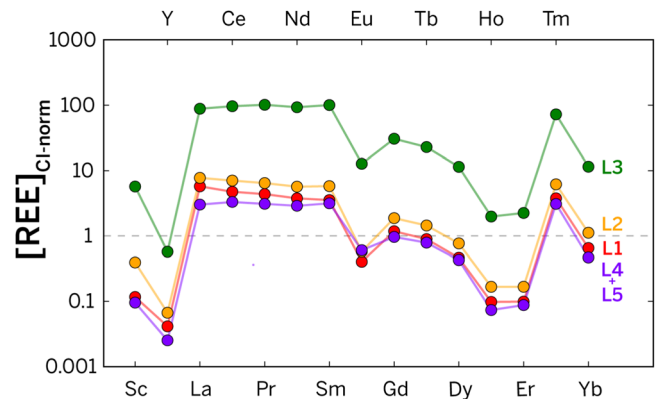

Figure 5. REE abundances in the different leachates from the fg-CAI *Ororo* normalized to the CI composition (Pourmand et al. 2012). Given the known affinity of REEs for co-precipitating as fluorides during HF-digestion (Yokoyama et al. 1999), the abundances for L4 and L5 were combined to avoid analytical artifacts associated with sample processing.

of matrix-derived material also falls short in explaining these patterns given the markedly low REE abundances in these components (Tanaka & Masuda 1973). The Allende matrix also exhibits a relatively flat REE pattern, which would dampen the Group II trend should it comprise a significant fraction of the fg-CAI REE budget. As such, it is more likely that the consistent Group II patterns across leachates reflect the multiple nebular recondensation events (Hashimoto & Grossman 1987; Krot et al. 2004) that were recorded in the silicate precursors of these secondary phases. It is worth noting that nebular processes may also contribute to the s-deficits observed in

Figure 4(c). Similar trends manifest in molybdenum isotope anomalies of cg-CAIs from various CV chondrites (Budde et al. 2023a), suggesting that s-deficit variability may also be a primary characteristic of the CAI-forming region.

To first order, these signatures combine to suggest that at some point in the complex history of fg-CAIs the early refractory condensates that compose these inclusions interacted with a reservoir enriched in supernova-derived materials. The timing of such interactions and the location of said reservoirs, however, are currently difficult to constrain.

4.3. An Isotopically Distinct Reservoir Sampled by Refractory Condensates

In contrast to the relatively well-defined trends observed in L1 and L3 (Section 4.1), no clear correlations are seen in the L4 and L5 leachates. This is unlikely to be an artifact of the slightly larger errors associated with measuring at lower voltages ($\sim$1.5 V on ^{138}Ba for most of the samples), as the L5 leachates of *Charles* and *Erik* (labeled *C* and *E* in Figures 4(d)–(f)), measured at the same intensity as those in L1 and L3 (i.e., 3 V on ^{138}Ba), lie well outside of the s-deficit trends.

Taken at face value, this implies that the L4 and L5 phases formed from a different reservoir compared to those sampled by L1 and L3. Considering the aforementioned s-variability in the Mo of cg-CAIs (Budde et al. 2023a), these signatures may signal a temporal shift in the composition of the CAI-forming region, with L4 and L5 representing its primitive signature prior to inputs from low-mass AGB stars. This interpretation of primitive condensates is not without precedent, as the absence of ^{26}Al in FUN CAIs (Lee et al. 1979) and PLACs (Liu et al. 2009) has also been suggested to be signatures that predate input from explosive nucleosynthesis, or at least represent reservoirs depleted of these stellar components.

Alternatively, the distinct trends in Ba isotope anomalies for L1/L3 versus L4/L5 may reflect the transport history of early refractory condensates. Most CAIs, especially larger examples, are observed in CC meteorites that are believed to have accreted in the outer solar system (Kleine et al. 2020). CAIs, however, are thought to have formed very close to the Sun (McKeegan et al. 2011), and so these early solids must have seen extensive transport in order to be incorporated in carbonaceous parent bodies. As discussed in Section 4.2, the secondary phases represented by these leachates may preserve signatures of nebular processing. In this "transport-only" end-member scenario, the precursors of L1 and L3 phases would sample the s-variability of the CC reservoir, and the composition of the CAI-forming region does not change. Reconciling such a static CAI-forming region composition with the s-variability of cg-CAIs requires the remelting of these inclusions to have occurred after transport, possibly through eruptive heating outbursts in the nascent nebula (Hu et al. 2021).

4.4. Decoupling of Nucleosynthetic Sr and Ba Signatures

Perhaps the most striking characteristic of the μ^{13x}Ba of L4 and L5 leachates is the absence of large anomalies akin to those previously observed for strontium isotopes (Charlier et al. 2021). For all L4 and L5 samples, the uncertainties for isotopes with r-process contributions (μ^{135}Ba, μ^{137}Ba, and μ^{138}Ba) are low enough ($<1‰$) to resolve excesses similar to that of μ^{84}Sr.

Assuming a single r-process for Sr and Ba with comparable production factors and similar magnitude anomalies (e.g., Type II supernovae; Rauscher et al. 2002), the absence of large excesses in these isotopes may be taken as support for the notion that the μ^{84}Sr of L4/L5 are true p-excesses (Charlier et al. 2021).

However, the p-process isotopes ^{130}Ba and ^{132}Ba also do not exhibit any large isotope anomalies. Taken on its own, the 9654 ppm uncertainty on the +10,019 ppm excess in ^{130}Ba for *Peter*'s L5 leachate (μ^{84}Sr = +5225) may be considered as a resolvable p-excess. However, it must be noted that this sample was measured at about half the voltage of the reference standard, and as such the quoted uncertainty may be underestimated. Furthermore, other samples with large reported μ^{84}Sr anomalies such as the L4 leachate of *Jean* (+18,474 ppm) and L5 leachate from *Ororo* (+11,599 ppm) do not exhibit the same supposed ^{130}Ba excesses despite having lower quoted uncertainties on μ^{130}Ba (+5145 and +235 ppm, respectively). Combined with the absence of resolvable μ^{132}Ba anomalies in the same sample (*Peter*), there appears to be a general absence of large p-excesses for barium. Overall, the barium isotope signatures shown here are unable to resolve the ambiguity in the true stellar nature of the L4 and L5 strontium isotope anomalies.

The lack of resolvable barium isotope anomalies may be explained by (1) the disparate effects from mixing of other stellar inputs or (2) the decoupling of stellar sources for the p-/r-nuclides of Ba and Sr. A possible example of the former is the effect of s-process carriers to the overall Ba and Sr budget. In general, mainstream SiC have 1–2 orders of magnitude higher barium concentrations than strontium (Amari et al. 1995). As such, vaporizing these carriers in the CAI-forming region would have a considerably larger effect on the isotope anomalies of barium relative to strontium. However, as discussed in Section 4.3, there does not appear to be a significant s-process contribution in the signatures of the most refractory leachates. This suggests that the effects of differential dilution of anomalies, at least those pertaining to addition of mainstream SiC, may be minimal.

Distinct stellar sources for refractory strontium and barium appear to be the best explanation for the observed μ^{13x}Ba anomalies. Indeed, Figure 6 shows that the μ^{84}Sr and μ^{137}Ba anomalies of these leach fractions are uncorrelated. Brennecka et al. (2013) also showed that at the bulk CAI level the patterns for isotope anomalies can be decoupled between light and heavy elements. One key observation in support of this hypothesis is the observed positive μ^{84}Sr anomalies in these CAIs that are accompanied by p- and/or r-depletions for Sm and Nd.

The decoupling of strontium and barium isotope anomalies may be explained by models for nucleosynthesis that predict a significantly higher production of Sr over Ba. It has recently been shown that accounting for stellar rotation can increase the yields of weak s-process nuclides in massive ($\sim$25 $M_\odot$), low-Z stars for $\sim$70 $< A <$ 140 (Pignatari et al. 2008). In turn, the increased availability of trans-iron seeds results in a comparable increase in p-nuclide yields (Choplin et al. 2022). In these scenarios, it is shown that the combined overproduction from hydrostatic and explosive burning is about an order of magnitude higher for Sr than for Ba.

The potential stellar environments that could produce such decoupled Sr and Ba signatures may also be gleaned from the
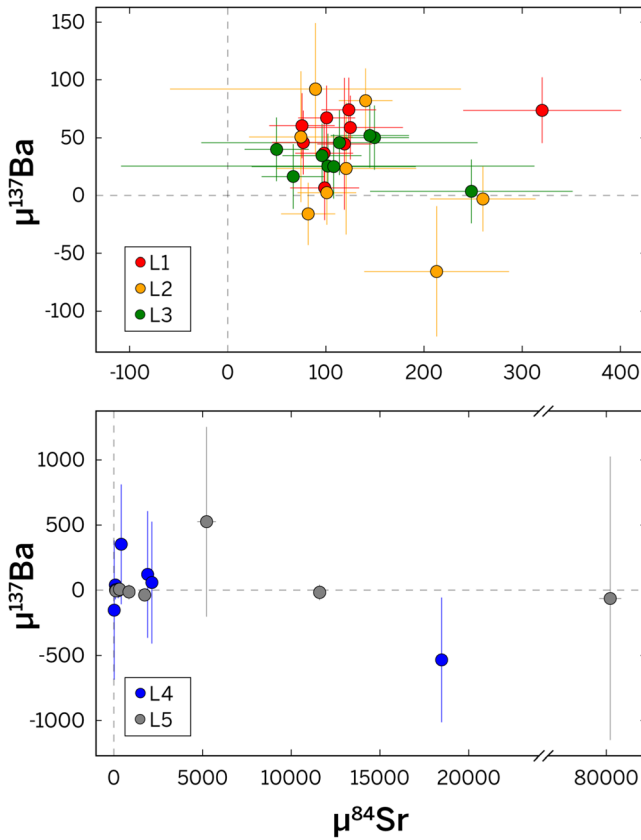
Figure 6. Strontium isotope anomalies (μ^{84}Sr) of leachates from Allende fg-CAIs from Charlier et al. (2021) plotted against barium isotope anomalies (μ^{137}Ba) of the same solutions as presented in this work. μ^{137}Ba anomalies are used here since other relatively abundant Ba isotopes (^{135}Ba and ^{138}Ba) may be influenced by radiogenic inputs from ^{135}Cs and ^{138}La decay, respectively. There is no correlation between the anomalies for Sr and Ba.

nucleosynthetic isotope systematics of other elements in refractory oxides. Recently, Nittler et al. (2018) discovered large ^{54}Cr anomalies, possibly accompanied by ^{50}Ti-excesses, in oxides from the Orgueil CI chondrite. These authors hypothesized that these signatures may have originated from either Type Ia supernovae or electron-capture supernovae (ECSNe). Type Ia scenarios fail to explain the decoupled strontium and barium anomalies, as both 2D delayed detonation and pure deflagration models predict comparable production of Sr and Ba p-nuclides (Travaglio et al. 2011). ECSNe are an intriguing explanation for our observations, as both 2D hydrodynamic calculations (Wanajo et al. 2013) and 3D deflagration simulations (Jones et al. 2019) predict significantly lower production factors (<0.001) for $A > 90$ owing to the lower electron-capture reaction rates of these heavier nuclides. In contrast, depending on the matter density, these models predict rather significant ^{84}Sr- and/or ^{88}Sr-excesses relative to the solar abundances (Lodders 2003). As such, the thermonuclear reactions during ECSNe appear to be capable of explaining the large μ^{84}Sr anomalies and minimal shifts in the Ba isotope composition of early condensates simultaneously.

5. Conclusions

In this work, we show how step leaching can reveal critical information regarding the origin and processing history of fg-CAIs and their components. By analyzing the nucleosynthetic Ba isotope anomalies (μ^{13x}Ba) of individual phases that constitute these inclusions, we are able to extract information that is often lost with traditional bulk processing. Here we propose that the barium isotope anomalies in leachates reflect shifts in the isotopic composition of reservoirs sampled by these different components, which may be due to (1) changes in the composition of the CAI-forming region, (2) transport of early condensates throughout the disk, and/or (3) alteration through parent-body processing. These processes are gleaned from the following observations:

1. Secondary phases digested in L1 and L3 follow s-process variations. However, the μ^{135}Ba anomalies in these same leachates necessitate an additional presolar end-component, which we propose to be a supernova-derived end-member with a composition akin to SiC X grains (Section 4.1).

2. Matrix-derived barium follows s-process variations, thus failing to explain the X-grain-like variability in L1 and L3 leachates. This suggests that nebular processing and recondensation must have a significant contribution to the barium isotope budget of fg-CAIs. The preservation of persistent Group II REE patterns across leachates supports this interpretation (Section 4.2).

3. The most refractory components of fg-CAIs (L4 and L5) do not appear to follow the same end-member variability observed in L1 and L3 leachates. This suggests a shift in the composition of the reservoirs sampled by the most primitive oxide/silicates and the precursors of secondary components. This observation is analogous to the marked increase in the magnitude of strontium isotope anomalies (μ^{84}Sr) toward the more refractory leachates (Section 4.3).

4. Unlike for μ^{84}Sr, barium p-nuclides (i.e., ^{130}Ba, ^{132}Ba) do not exhibit large isotope anomalies, invoking a stellar source in which Sr nucleosynthesis and Ba nucleosynthesis are decoupled. We rule out Type Ia supernovae as a possible source given the comparable production of these elements in these scenarios. Rotating massive stars undergoing core-collapse supernovae pose as possible sites that can produce the observed Sr and Ba decoupling. Similarly, ECSNe offer a viable explanation, as the low electron-capture reaction rates for nuclides with $A > 90$ preclude significant production of barium in these stellar environments (Section 4.4).

Our observations on fg-CAI components provide significant constraints with regard to our interpretation and understanding of ESS disk dynamics and its stellar building blocks. Specifically, models that describe the transport of material within the nebula and pollution from nearby stars must account for how these processes would manifest in different parts of the disk and be recorded in early condensates. Because the Ba isotopic anomalies described here are anchored to the mineralogy and texture of these refractory inclusions, these observations also provide information regarding the relative timing of disk processes and stellar inputs represented by these nucleosynthetic signatures.

Acknowledgments

Appendix

A.1. Number of Principal Components to Explain $\mu^{13\,x}$Ba Variability

In order to evaluate the contributions of possible presolar end-members to the Ba isotope anomalies of fg-CAIs, we consider a three-dimensional space defined by μ^{135}Ba, μ^{137}Ba, and μ^{138}Ba. To get a sense of the number of components required to describe the variance in the data, we perform a routine principal component analysis (PCA) on the non-mean-centered data matrix containing our measurements, denoted here as the $3 \times m$ matrix $\boldsymbol{B}$ for m samples:

$$\boldsymbol{B} = \begin{bmatrix} \mu^{135}\mathrm{Ba}_1 & \mu^{135}\mathrm{Ba}_2 & \cdots & \mu^{135}\mathrm{Ba}_m \\ \mu^{137}\mathrm{Ba}_1 & \mu^{137}\mathrm{Ba}_2 & \cdots & \mu^{137}\mathrm{Ba}_m \\ \mu^{138}\mathrm{Ba}_1 & \mu^{138}\mathrm{Ba}_2 & \cdots & \mu^{138}\mathrm{Ba}_m \end{bmatrix}.$$

Here we use singular value decomposition to factorize $\boldsymbol{B}$ such that

$$\boldsymbol{B} = \boldsymbol{U}\boldsymbol{\Sigma}\boldsymbol{V}^*,$$

where U contains the hierarchically arranged principal components,

$$\boldsymbol{U} = \begin{bmatrix} \vdots & \vdots & \vdots \\ p_1 & p_2 & p_3 \\ \vdots & \vdots & \vdots \end{bmatrix} = \begin{bmatrix} -0.7150 & -0.4959 & 0.4928 \\ -0.6451 & 0.1960 & -0.7386 \\ -0.2697 & 0.8460 & 0.4600 \end{bmatrix},$$

and Σ is a diagonal matrix containing the eigenvalues σ_n,

$$\boldsymbol{\Sigma} = \begin{bmatrix} \sigma_1 & 0 & 0 \\ 0 & \sigma_2 & 0 \\ 0 & 0 & \sigma_3 \end{bmatrix} = \begin{bmatrix} 303.1950 & 0 & 0 \\ 0 & 126.8359 & 0 \\ 0 & 0 & 41.8346 \end{bmatrix}.$$

These values can then be used to calculate the percentage of the total variance explained by each component:

$$\%\mathrm{var}_p = \sigma_p^2 \Big/ \sum_{i=1}^n \sigma_i^2.$$

From this, we see that the first two components p_1 and p_2 explain nearly all of the variance in the data (83.8% and 14.7%, respectively). As such, we can conclude that two components should suffice to explain most of the variance in barium isotope anomalies of L1 and L3 leachates. Put another way, one may interpret this to mean that the L1 and L3 anomalies approximately define a plane within the μ^{135}Ba-μ^{137}Ba-μ^{138}Ba space.

A.2. Variance Independent of s-process Contributions

A key issue with applying PCA to problems involving end-member mixing is the ambiguity with the physical meaning of the calculated principal components. That is, although a linear combination of principal component vectors p_1 and p_2 can mathematically reproduce our measurements, this gives us no insight regarding the contribution of certain nucleosynthetic end-members and/or physical processes in the isotopic signatures we observe. This is mainly because, by construction, PCA simply looks for the direction(s) of maximum variance within the data. For a two-component mixture, the resulting principal components would only correspond to actual presolar end-members in the highly unlikely scenario that their compositions are orthogonal in the μ^{135}Ba-μ^{137}Ba-μ^{138}Ba space.

Here we present an alternative approach to finding the presolar end-members that contribute to the nucleosynthetic Ba isotope anomalies of fg-CAI components. First, we make the assumption that there is a significant s-process contribution to the L1 and L3 compositions. We believe this assumption to be warranted, given the following:

1. The Ba isotopic composition of the Allende matrix (Budde et al. 2016) appears to follow that of mainstream SiC grains (Figure 4). Any remobilized Ba from the matrix reflected in the L1 and L3 leachates should then lie along the s- variation line. Indeed, secondary alteration products such as nepheline, sodalite, and hedenbergite, which appear to dissolve in L1 and L3 (see Table 2), are known to have formed from aqueous parent-body processing (Krot et al. 1995; MacPherson & Krot 2002) and in part should be composed of matrix-derived Ba.

2. Variability in s-deficits appears to manifest not only in the Mo isotope anomalies of bulk meteorites (i.e., Kleine et al. 2020) but also in bulk cg-CAIs (Budde et al. 2023a). Given the similarity in the reconstituted bulk $\mu^{13\,x}$Ba of fg-CAIs to that of bulk cg-CAIs (Figure 3), it is reasonable to expect s-variability in L1 and L3 leachates, as these constitute most of the total barium budget of these inclusions.

The following calculations aim to identify the composition of a supposed second component to account for the variability that cannot be explained by s-process contributions. Geometrically, this can be done by removing the s-process signatures through the rotation of the internally normalized mainstream SiC composition, denoted as the vector $s = [\mu^{135}\mathrm{Ba}_s \; \mu^{137}\mathrm{Ba}_s \; \mu^{138}\mathrm{Ba}_s]$, such that it becomes one of the basis vectors in a new vector space. To do so, we need an orthonormal basis that contains the normalized vector $\hat{s}$:

$$\hat{s} = \frac{s}{\|s\|}.$$

We use the Gram–Schmidt algorithm to orthornormalize the nonorthogonal set $\{\hat{i}, \hat{j}, \hat{s}\}$ to derive the transformation matrix, $\boldsymbol{A}$:

$$\boldsymbol{A} = \begin{bmatrix} 0.5963 & 0 & -0.8028 \\ -0.6542 & 0.5796 & -0.4859 \\ -0.4653 & -0.8149 & -0.3456 \end{bmatrix}.$$

Notice that the values in the last column of $\boldsymbol{A}$ are simply the elements of $\hat{s}$, representing the normalized mainstream SiC composition (Stephan et al. 2019). With this transformation matrix, the data matrix can be rotated such that the s-process vector is oriented along the new z-direction, $\hat{k}'$. More specifically, multiplying the transpose of $\boldsymbol{A}$ allows us to get $\boldsymbol{B}'$, which is simply the original data matrix $\boldsymbol{B}$ expressed in our

s-process-derived orthonormal basis:

$$\boldsymbol{B}' = \boldsymbol{A}^{-1}\boldsymbol{B}.$$

Since we have assigned s-variations to follow the $\hat{k}'$ direction, we can reperform the singular value decomposition on the components along the $\hat{i}'$ and $\hat{j}'$ direction of our new basis to derive a component that can explain variations orthogonal to s-variability:

$$\boldsymbol{B}'_{ij} = \boldsymbol{U}'_{ij}\boldsymbol{\Sigma}'_{ij}\boldsymbol{V}^{*'}_{ij},$$

where $\boldsymbol{U}'_{ij}$ is now a 2×2 unitary matrix that contains the $\hat{i}'$ and $\hat{j}'$ coordinates of principal components perpendicular to the s-process vector. We calculate that

$$\boldsymbol{U}'_{ij} = \begin{bmatrix} 0.8272 & -0.5619 \\ 0.5619 & 0.8272 \end{bmatrix}, \ \boldsymbol{\Sigma}'_{ij} = \begin{bmatrix} 126.8790 & 0 \\ 0 & 72.1716 \end{bmatrix}.$$

This means that a vector with components [0.8272 0.5619 0] in our s-derived basis, assigned here as $\hat{c}'$, can explain 75.55% of the remaining variance that is not associated with s-variability. To convert this back to actual μ^{13x}Ba anomalies, we simply calculate the unrotated vector equivalent, $\hat{c}$:

$$\hat{c} = \boldsymbol{A}\hat{c}' = \begin{bmatrix} \mu^{135}\mathrm{Ba}_{P_A} \\ \mu^{137}\mathrm{Ba}_{P_A} \\ \mu^{138}\mathrm{Ba}_{P_A} \end{bmatrix} = \begin{bmatrix} 0.4936 \\ -0.2184 \\ -0.8418 \end{bmatrix}.$$

A.3. Identifying an End-member to Explain Non-s-variability

So far, the vectors that we have identified to explain the observed μ^{13x}Ba variability (i.e., $\hat{s}$ and $\hat{c}$) are still orthogonal by construction. As previously stated, such orthogonality of end-member compositions is not necessary in order to explain the L1 and L3 signatures. However, we can use these calculations to assess the viability of known presolar signatures in explaining the observed variance in Ba isotope anomalies. Here we consider an ideal end-member to have an isotopic signature, represented here as $\hat{d}$, that lies on the 2D plane defined by $\hat{s}$ and $\hat{c}$. Mathematically, this translates to:

$$\hat{d} \cdot (\hat{s} \times \hat{c}) = 0.$$

Since all of these vectors are normalized, this dot product also allows us to quantitatively compare different candidate end-members for explaining our isotope anomaly data. Here we assessed SiC X grains (Stephan et al. 2018) as possible end-members, which are presolar grains with isotopic signatures derived from explosive nucleosynthesis. In addition, we also evaluate the predicted Ba isotope composition from Type II supernova scenarios based on the models from Rauscher et al. (2002) via Stephan et al. (2018).

Figure A1 shows that both X1 and X2 grains, as well as their corresponding Type II supernova model fits, lie on the plane defined by our Ba isotope data and the s-process variability vector within uncertainty (i.e., $\hat{d} \cdot (\hat{s} \times \hat{c}) \sim 0$). This suggests that the reservoir sampled by phases dissolved during L1 and L3 (or the precursors thereof) may have had significant contributions from explosive nucleosynthesis.

A.4. Possible Effects of Nonexponential Mass-dependent Fractionation

In addition to presolar SiC X grains, we also evaluated the possibility of nonexponential mass-dependent isotope effects as
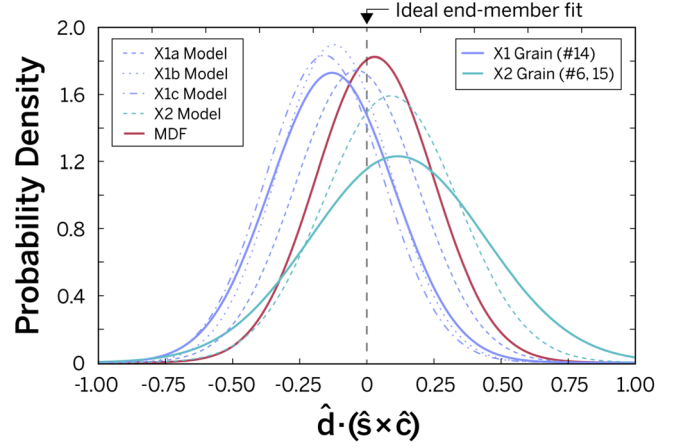

Figure A1. Fit of various candidate end-members for explaining the non-s-process variability in μ^{135}Ba-μ^{137}Ba-μ^{138}Ba anomalies of fg-CAI leaching fractions. The fit is evaluated based on the coplanarity of the end-member vector ($\hat{d}$) to the plane defined by the normalized s-process composition ($\hat{s}$) and the orthonormal vector along the maximal residual variance ($\hat{c}$). End-member compositions are based on SiC X-grain measurements and Type II supernova model fits from Stephan et al. (2018). Spurious Ba isotope anomalies resulting from nonexponential mass-dependent fractionation (MDF; in red) are also evaluated here as a possible source of non-s-variability.

a source of the non-s-variability in fg-CAI leachates. It has been demonstrated that spurious isotope anomalies can arise from the inaccurate correction of natural and analytical mass-dependent isotope fractionation (Zhang et al. 2014; Davis et al. 2015; Budde et al. 2023b). Calculating for nucleosynthetic isotope anomalies often involves corrections for mass-dependent effects using the exponential law owing to its suitability for correcting instrumental fractionation (Russell et al. 1978). As such, a sample that has undergone extensive *natural* fractionation that does not follow the exponential law (e.g., equilibrium fractionation, Rayleigh distillation) would result in erroneously calculated anomalies. These spurious anomalies ($d\mu$) can be calculated for any isotope in the system (here for isotope c as an example) and are proportional to the fractionation on the ratio of normalizing isotopes b and a ($\delta'_{b/a}$):

$$d\mu_{c/a} = 1000 \cdot (\Theta^{\mathrm{exp}}_{c/a-b/a} - \Theta^{\mathrm{true}}_{c/a-b/a}) \cdot \delta'_{b/a},$$

where Θ is the mass fractionation exponent (Dauphas & Schauble 2016; Tissot et al. 2023). This term denotes the relative difference in masses between the isotope of interest and the normalizing isotopes after scaling with the generalized power law the exponent n, which is a free parameter that is distinct for each type of fractionation law (Maréchal et al. 1999):

$$\Theta^{f(n)}_{c/a-b/a} = \frac{m_c^n - m_a^n}{m_b^n - m_a^n}.$$

With this, we can derive a vector that describes the relative proportion of spurious anomalies in each Ba isotope from nonexponential fractionation. Here we show that, similar to X grains, this vector also lies within the plane defined by $\hat{s}$ and $\hat{c}$ (mass-dependent fractionation; Figure A1). This suggests that if we only consider the orientation of these end-member compositions within the μ^{135}Ba-μ^{137}Ba-μ^{138}Ba space, both mass-dependent fractionation and supernova-derived signatures
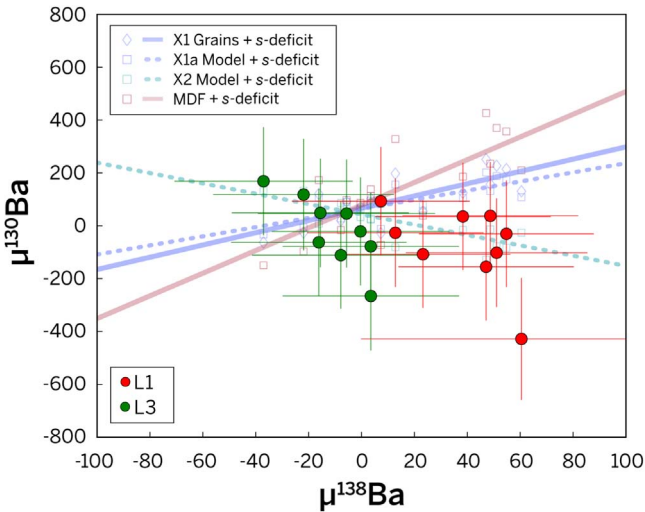
Figure A2. Evaluation of end-member candidates for explaining the non-*s*-process variability in $\mu^{13\,x}$Ba of fg-CAI leaching fractions based on their predicted anomalies in the μ^{138}Ba vs. μ^{130}Ba space. Eigenvalues for each end-member scenario were derived via the μ^{135}Ba and μ^{137}Ba anomaly data and were then used to calculate predicted μ^{130}Ba values (open diamonds for the X1 grain, open squares for Type II supernova models and nonexponential mass-dependent fractionation). A simple linear regression was performed on these hypothetical data points to assess the general trend predicted by each end-member scenario. The X2 Type II supernova model is the only scenario that is able to reproduce the negative μ^{138}Ba vs. μ^{130}Ba correlation.

pose an equally viable case for explaining the variations in the our Ba isotope data.

To resolve this ambiguity, we examine the nucleosynthetic isotope anomalies on the *p*-nuclide ^{130}Ba. There appears to be a slightly negative correlation between μ^{130}Ba and the anomalies on the major isotope, μ^{138}Ba (Figure A2). We can then calculate the predicted μ^{130}Ba anomalies from mixing X-grain-like signatures versus mass-dependent fractionation and compare the trends from these predicted anomalies with the observed μ^{130}Ba versus μ^{138}Ba correlation as a means to evaluate these scenarios.

First, we calculate the relative contribution of the *s*-process end-member and the supposed second component for each sample. For each end-member *i*, we can use its predicted μ^{135}Ba and μ^{137}Ba anomalies and that of mainstream SiC to solve for their respective eigenvalues:

$$\begin{bmatrix} \lambda_i \\ \lambda_s \end{bmatrix} = \begin{bmatrix} \mu^{135}\text{Ba}_i & \mu^{135}\text{Ba}_s \\ \mu^{137}\text{Ba}_i & \mu^{137}\text{Ba}_s \end{bmatrix}^{-1} \begin{bmatrix} \mu^{135}\text{Ba}_{\text{samp}} \\ \mu^{137}\text{Ba}_{\text{samp}} \end{bmatrix}.$$

It is important to be mindful that, because of the nonorthogonality of these supposed end-member compositions and the *s*-process vector, the calculated value of λ_s can vary significantly for each scenario. The predicted anomalies on ^{130}Ba for each candidate end-member can be calculated using their respective μ^{130}Ba$/\mu^{135}$Ba or μ^{130}Ba$/\mu^{137}$Ba ratio:

$$\mu^{130}\text{Ba}_{\text{predicted}} = \begin{bmatrix} \dfrac{\mu^{130}\text{Ba}_i}{\mu^{135}\text{Ba}_i} & \dfrac{\mu^{130}\text{Ba}_s}{\mu^{135}\text{Ba}_s} \end{bmatrix} \begin{bmatrix} \lambda_i \\ \lambda_s \end{bmatrix}$$
$$= \begin{bmatrix} \dfrac{\mu^{130}\text{Ba}_i}{\mu^{137}\text{Ba}_i} & \dfrac{\mu^{130}\text{Ba}_s}{\mu^{137}\text{Ba}_s} \end{bmatrix} \begin{bmatrix} \lambda_i \\ \lambda_s \end{bmatrix}.$$

In Figure A2, we plot the predicted μ^{130}Ba anomalies from scenarios that involve end-member compositions akin to that of X1 grains, X1a and X2 model predictions, and spurious

anomalies from mass-dependent fractionation. A simple linear regression was performed on the resulting data in order to assess the general trend predicted for each end-member scenario. We see that only the X2 model is able to reproduce the slight negative trend observed in our actual L1 and L3 data (note that both X2 grains #6 and #15 in Stephan et al. 2018 did not have any presented μ^{130}Ba or μ^{132}Ba data, likely due to the extremely low counts for these isotopes). Spurious anomalies from nonexponential mass-dependent fractionation result in a notably poor replication of the observed μ^{130}Ba versus μ^{138}Ba trend, producing a positive slope that is in stark contrast to the data. As such, we rule out nonexponential mass-dependent fractionation as a primary contributor to the observed variance in the barium isotope anomalies of these fg-CAI leachates.

ORCID iDs

R. T. C. Marquez https://orcid.org/0000-0002-8317-9397
B. L. A. Charlier https://orcid.org/0000-0003-0285-8978
F. L. H. Tissot https://orcid.org/0000-0001-6622-2907

References

Amari, S., Hoppe, P., Zinner, E., & Lewis, R. S. 1992, ApJL, 394, L43
Amari, S., Hoppe, P., Zinner, E., & Lewis, R. S. 1995, Metic, 30, 679
Bouvier, A., & Wadhwa, M. 2010, NatGe, 3, 637
Brennecka, G. A., Borg, L. E., & Wadhwa, M. 2013, PNAS, 110, 17241
Brennecka, G. A., Burkhardt, C., Budde, G., et al. 2020, Sci, 370, 837
Budde, G., Burkhardt, C., Brennecka, G. A., et al. 2016, E&PSL, 454, 293
Budde, G., Marquez, R., Ivanova, M., & Tissot, F. 2023a, LPICo, 2806, 2203
Budde, G., Tissot, F. L., Kleine, T., & Marquez, R. T. 2023b, Geoch, 83, 126007
Charlier, B. L. A., Ginibre, C., Morgan, D., et al. 2006, ChGeo, 232, 114
Charlier, B. L. A., Tissot, F., Dauphas, N., & Wilson, C. 2019, GeCoA, 265, 413
Charlier, B. L. A., Tissot, F. L. H., Vollstaedt, H., et al. 2021, SciA, 7, eabf6222
Choplin, A., Goriely, S., Hirschi, R., Tominaga, N., & Meynet, G. 2022, A&A, 661, A86
Connelly, J. N., Bizzarro, M., Krot, A. N., et al. 2012, Sci, 338, 651
Craig, G., Hu, Z., Zhang, A., et al. 2017, Thermo Fish. Sci., Tech. Note 30396
Crozaz, G., Floss, C., & Wadhwa, M. 2003, GeCoA, 67, 4727
Dauphas, N., & Schauble, E. A. 2016, AREPS, 44, 709
Davis, A. M. 2011, PNAS, 108, 19142
Davis, A. M., & Grossman, L. 1979, GeCoA, 43, 1611
Davis, A. M., Richter, F. M., Mendybaev, R. A., et al. 2015, GeCoA, 158, 245
Deniel, C., & Pin, C. 2001, Analytica Chimica Acta, 426, 95
Desch, S. J., Dunlap, D. R., Dunham, E. T., Williams, C. D., & Mane, P. 2023, Icar, 402, 115607
Hashimoto, A., & Grossman, L. 1987, GeCoA, 51, 1685
Hoppe, P., & Ott, U. 1997, in AIP Conf. Proc. 402, Astrophysical implications of the laboratory study of presolar materials, ed. T. J. Bernatowicz & E. Zinner (Melville, NY: AIP), 27
Hoppe, P., Strebel, R., Eberhardt, P., Amari, S., & Lewis, R. S. 2000, M&PS, 35, 1157
Horwitz, E., Dietz, M., & Chiarizia, R. 1992, JRNC, 161, 575
Hu, J., Dauphas, N., Tissot, F., et al. 2021, SciA, 7, eabc2962
Jones, S., Röpke, F., Fryer, C., et al. 2019, A&A, 622, A74
Kita, N. T., Yin, Q.-Z., MacPherson, G. J., et al. 2013, M&PS, 48, 1383
Kleine, T., Budde, G., Burkhardt, C., et al. 2020, SSRv, 216, 1
Kondev, F., Wang, M., Huang, W., Naimi, S., & Audi, G. 2021, ChPhC, 45, 030001
Krot, A. N., MacPherson, G. J., Ulyanov, A. A., & Petaev, M. I. 2004, M&PS, 39, 1517
Krot, A. N., Scott, E. R., & Zolensky, M. E. 1995, Metic, 30, 748
Larsen, K., Wielandt, D., Schiller, M., Krot, A., & Bizzarro, M. 2020, E&PSL, 535, 116088
Lee, T., Russell, W. A., & Wasserburg, G. 1979, ApJL, 228, L93
Lichtenberg, T., Drążkowska, J., Schönbächler, M., Golabek, G. J., & Hands, T. O. 2021, Sci, 371, 365
Liu, M.-C., McKeegan, K. D., Goswami, J. N., et al. 2009, GeCoA, 73, 5051

Lodders, K. 2003, ApJ, 591, 1220
MacPherson, G., & Krot, A. 2002, M&PS, 37, A91
Maréchal, C. N., Télouk, P., & Albarède, F. 1999, ChGeo, 156, 251
Mason, B., & Taylor, S. R. 1982, SmCES, 25, 1
Masuda, Y., & Yokoyama, T. 2023, GeCoA, 345, 50
McKeegan, K., Kallio, A., Heber, V., et al. 2011, Sci, 332, 1528
Morbidelli, A., Baillie, K., Batygin, K., et al. 2022, NatAs, 6, 72
Moynier, F., Day, J. M., Okui, W., et al. 2012, ApJ, 758, 45
Nittler, L. R., Alexander, C. M., Liu, N., & Wang, J. 2018, ApJL, 856, L24
Nittler, L. R., & Ciesla, F. 2016, ARA&A, 54, 53
Pignatari, M., Gallino, R., Meynet, G., et al. 2008, ApJL, 687, L95
Pourmand, A., Dauphas, N., & Ireland, T. J. 2012, ChGeo, 291, 38
Rauscher, T., Heger, A., Hoffman, R., & Woosley, S. 2002, ApJ, 576, 323

Russell, W., Papanastassiou, D., & Tombrello, T. 1978, GeCoA, 42, 1075
Shollenberger, Q. R., Borg, L. E., Render, J., et al. 2018, GeCoA, 228, 62
Stephan, T., Trappitsch, R., Davis, A. M., et al. 2018, GeCoA, 221, 109
Stephan, T., Trappitsch, R., Hoppe, P., et al. 2019, ApJ, 877, 101
Stolper, E., & Paque, J. M. 1986, GeCoA, 50, 1785
Tanaka, T., & Masuda, A. 1973, Icar, 19, 523
Tissot, F. L., Ibañez-Mejia, M., Rabb, S. A., et al. 2023, JAAS, 38, 2087
Travaglio, C., Röpke, F., Gallino, R., & Hillebrandt, W. 2011, ApJ, 739, 93
Wanajo, S., Janka, H.-T., & Müller, B. 2013, ApJL, 767, L26
Warren, P. H. 2011, E&PSL, 311, 93
Yap, T. E., & Tissot, F. L. 2023, Icar, 405, 115680
Yobregat, E., Fitoussi, C., & Bourdon, B. 2017, JAAS, 32, 1388
Yokoyama, T., Makishima, A., & Nakamura, E. 1999, ChGeo, 157, 175
Zhang, J., Huang, S., Davis, A. M., et al. 2014, GeCoA, 140, 365